PHYSICAL REVIEW D **92,** 112009 (2015)

Model-independent confirmation of the $Z(4430)^-$ state

R. Aaij *et al.*[*]
(LHCb Collaboration)

(Received 8 October 2015; published 29 December 2015)

The decay $B^0 \to \psi(2S)K^+\pi^-$ is analyzed using 3 fb^{-1} of pp collision data collected with the LHCb detector. A model-independent description of the $\psi(2S)\pi$ mass spectrum is obtained, using as input the $K\pi$ mass spectrum and angular distribution derived directly from data, without requiring a theoretical description of resonance shapes or their interference. The hypothesis that the $\psi(2S)\pi$ mass spectrum can be described in terms of $K\pi$ reflections alone is rejected with more than 8σ significance. This provides confirmation, in a model-independent way, of the need for an additional resonant component in the mass region of the $Z(4430)^-$ exotic state.

DOI: 10.1103/PhysRevD.92.112009 PACS numbers: 14.40.Rt, 12.39.Mk, 13.25.Hw, 14.40.Nd

I. INTRODUCTION

Almost all known mesons and baryons can be described in the quark model with combinations of two or three quarks, although the existence of higher multiplicity configurations, as well as additional gluonic components, is, in principle, not excluded [1]. For many years, significant effort has been devoted to the search for such exotic configurations. In the baryon sector, resonances with a five-quark content have been searched for extensively [2–5]. Recently, LHCb has observed a resonance in the $J/\psi p$ channel, compatible with being a pentaquark-charmonium state [6]. In the meson sector, several charmoniumlike states, that could be interpreted as four-quark states [7,8], have been reported by a number of experiments, but not all of them have been confirmed.

The existence of the $Z(4430)^-$ hadron, originally observed by the Belle Collaboration [9–11] in the decay $B^0 \to K^+Z(4430)^-$ with $Z(4430)^- \to \psi(2S)\pi^-$, was confirmed by the LHCb Collaboration [12] (the inclusion of charge-conjugate processes is implied). This state, having a minimum quark content of $c\bar{c}u\bar{d}$, is the strongest candidate for a four-quark meson [13–24]. Through a multidimensional amplitude fit, LHCb confirmed the existence of the $Z(4430)^-$ resonance with a significance of 13.9σ, and its mass and width were measured to be $M_{Z^-} = 4475 \pm 7^{+15}_{-25}$ MeV$/c^2$ and $\Gamma_{Z^-} = 172 \pm 13^{+37}_{-34}$ MeV$/c^2$. Spin parity of $J^P = 1^+$ was favored over the other assignments by more than 17.8σ, and through the study of the variation of the phase of the $Z(4430)^-$ with mass, LHCb demonstrated its resonant character.

The *BABAR* Collaboration [25] searched for the $Z(4430)^-$ state in a data sample statistically comparable to Belle's. They used a model-independent approach to test whether an interpretation of the experimental data is possible in terms of the known resonances in the $K\pi$ system. The $K\pi$ mass and angular distributions were determined from data and used to predict the observed $\psi(2S)\pi$ mass spectrum. It was found that the observed $\psi(2S)\pi$ mass spectrum was compatible with being described by reflections of the $K\pi$ system. Therefore, no clear evidence for a $Z(4430)^-$ was established, although *BABAR*'s analysis did not exclude the observation by Belle.

The present article describes the details of an LHCb analysis that was briefly reported in Ref. [12]. Adopting a model-independent approach, along the lines of *BABAR*'s strategy, the structures observed in the $\psi(2S)\pi$ mass spectrum are predicted in terms of the reflections of the $K\pi$ system mass and angular composition, without introducing any modelling of the resonance line shapes and their interference patterns. The compatibility of these predictions with data is quantified.

II. LHCb DETECTOR

The LHCb detector [26,27] is a single-arm forward spectrometer covering the pseudorapidity range $2 < \eta < 5$, designed for the study of particles containing b or c quarks. The detector includes a high-precision tracking system consisting of a silicon-strip vertex detector surrounding the pp interaction region [28], a large-area silicon-strip detector located upstream of a dipole magnet with a bending power of about 4 Tm, and three stations of silicon-strip detectors and straw drift tubes [29] placed downstream of the magnet. The tracking system provides a measurement of momentum, p, of charged particles with a relative uncertainty that varies from 0.5% at low momentum to 1.0% at 200 GeV$/c$. The minimum distance of a track to a primary vertex, the impact parameter, is measured with a resolution of $(15 + 29/p_{\mathrm{T}})$ μm, where p_{T} is the component of the momentum transverse to the beam, in GeV$/c$. Different types of charged hadrons are distinguished using

[*]Full author list given at the end of the article.

information from two ring-imaging Cherenkov detectors [30]. Photons, electrons, and hadrons are identified by a calorimeter system consisting of scintillating-pad and preshower detectors, an electromagnetic calorimeter, and a hadronic calorimeter. Muons are identified by a system composed of alternating layers of iron and multiwire proportional chambers [31]. The online event selection is performed by a trigger [32], which consists of a hardware stage, based on information from the calorimeter and muon systems, followed by a software stage, which applies a full event reconstruction.

III. DATA SAMPLES AND CANDIDATE SELECTION

The results presented in this paper are based on data from pp collisions collected by the LHCb experiment, corresponding to integrated luminosities of 1 and 2 fb^{-1} at center-of-mass energies of 7 TeV in 2011 and 8 TeV in 2012, respectively.

In the simulation, pp collisions are generated using PYTHIA [33] with a specific LHCb configuration [34]. The decays of hadronic particles are described by EvtGen [35], in which final-state radiation is generated using PHOTOS [36]. The interaction of the generated particles with the detector, and its response, are implemented using the GEANT4 toolkit [37] as described in Ref. [38]. Samples of simulated events, generated with both 2011 and 2012 conditions, are produced for the decay $B^0 \to \psi(2S)K^+\pi^-$ with a uniform three-body phase-space distribution and the $\psi(2S)$ decaying into two muons. These simulated events are used to tune the event selection and for efficiency and resolution studies.

The selection is similar to that used in Ref. [12] and consists of a cut-based preselection followed by a multivariate analysis. Track-fit quality and particle identification requirements are applied to all charged tracks. The B^0 candidate reconstruction starts by requiring two well-identified muons, with opposite charges, having $p_{\mathrm{T}} > 2$ GeV/c and forming a good quality vertex. The dimuon invariant mass has to lie in the window 3630–3734 MeV/c^2, around the $\psi(2S)$ mass. To obtain a B^0 candidate, each dimuon pair is required to form a good vertex with a kaon and a pion candidate, with opposite charges. Pions and kaons are required to be inconsistent with coming from any primary vertex (PV) and to have tranverse momenta greater than 200 MeV/c.

The B^0 candidate has to have $p_{\mathrm{T}} > 2$ GeV/c, a reconstructed decay time exceeding 0.25 ps, and an invariant mass in the window 5200–5380 MeV/c^2 around the nominal B^0 mass. Contributions from $\phi \to K^+K^-$ decay, where one of the kaons is misidentified as a pion, are removed by vetoing the region 1010–1030 MeV/c^2 of the dihadron invariant mass calculated assuming that the π^- candidate has the K^- mass.

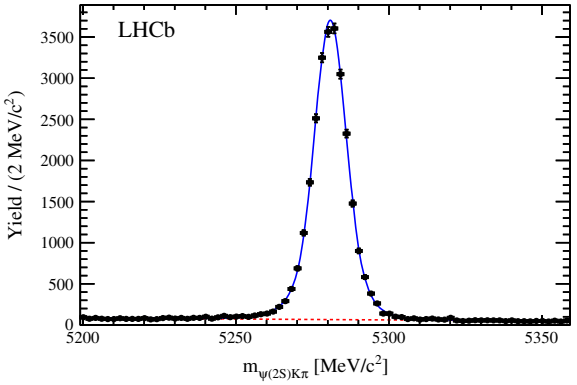

FIG. 1 (color online). Spectrum of the $\psi(2S)K\pi$ system invariant mass. Black dots are the data, the continuous (blue) line represents the fit result, and the dashed (red) line represents the background component.

To reduce the combinatorial background, a requirement is imposed on the output of a multivariate discriminator based on the likelihood ratio [39].

The four variables used as input are the smaller χ^2_{IP} of the kaon and the pion, where χ^2_{IP} is the difference in the PV fit χ^2 with and without the track under consideration; the $\mu^+\mu^-K\pi$ vertex-fit quality; the B^0 candidate impact parameter significance with respect to the PV; and the cosine of the largest opening angle between the $\psi(2S)$ and each of the charged hadrons in the plane transverse to the beam. After the multivariate selection, the B^0 candidate invariant-mass distribution appears as shown in Fig. 1 with a fitted curve superimposed. The fit model consists of a Hypatia distribution [40] to describe the signal and an exponential function to describe the background.

Table I provides the fit results and the signal and background yields in the signal region. The width of the distribution, σ_{B^0}, is defined as half the symmetric interval around M_{B^0} containing 68.7% of the total signal. The signal region is defined by the $\pm 2\sigma_{B^0}$ interval around M_{B^0}.

Sideband subtraction is used to remove the background which is dominated by combinations of $\psi(2S)$ mesons from b-hadron decays with random kaons and pions. Sidebands are identified by the intervals $[M_{B^0} - 80, M_{B^0} - 7\sigma_{B^0}]$ MeV/c^2 and $[M_{B^0}+7\sigma_{B^0}, M_{B^0}+80]$MeV/$c^2$. A weight, W_{signal}, is attributed to each candidate: unit

TABLE I. Results of the fit to the invariant mass spectrum of the $\psi(2S)K\pi$ system. The signal and the background yields are calculated in the signal region defined by the interval of $\pm 2\sigma_{B^0}$ around M_{B^0}.

Variable	Fit results
M_{B^0}	5280.83 ± 0.04 MeV/c^2
σ_{B^0}	5.77 ± 0.05 MeV/c^2
Signal yield	$23,801 \pm 158$
Background yield	757 ± 14

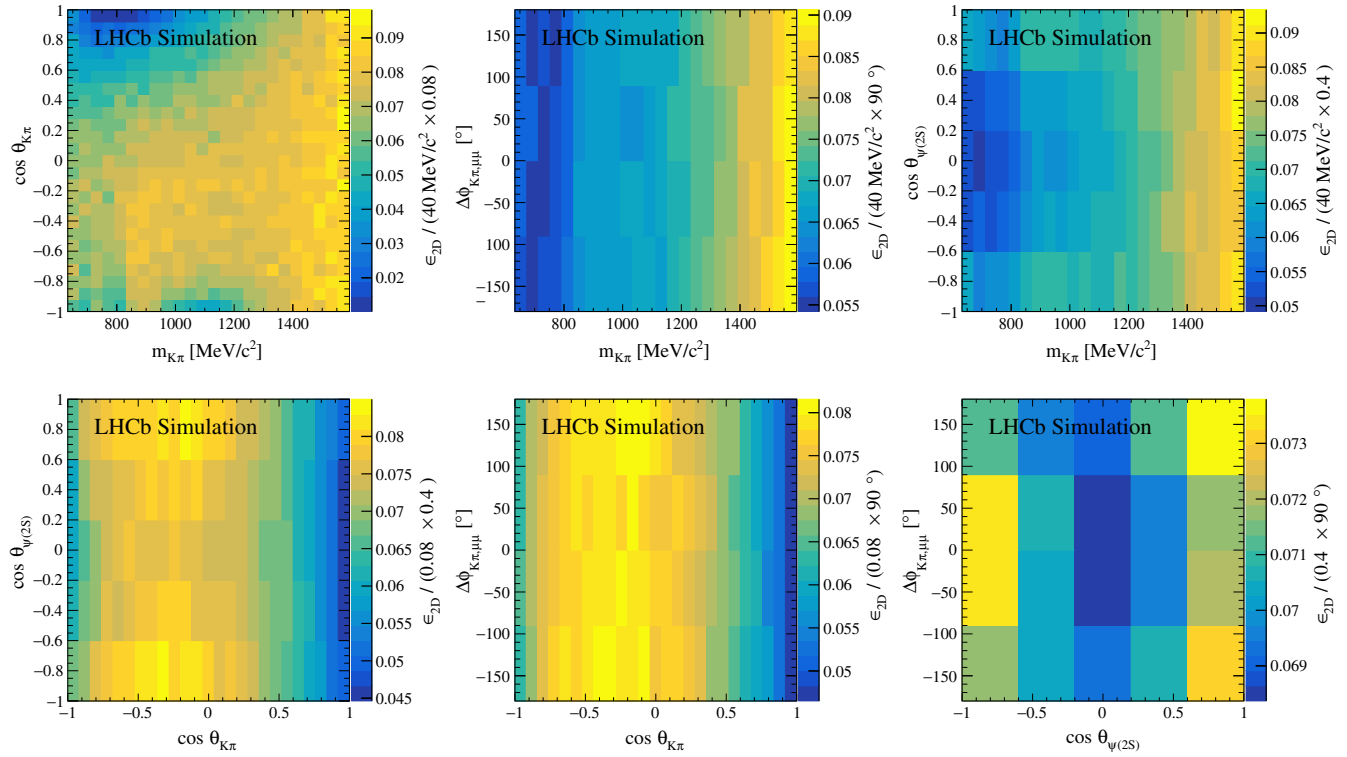

FIG. 2 (color online). The 2D efficiency is shown in the following planes: (top left) $(m_{K\pi}, \cos\theta_{K^{*0}})$, (top middle) $(m_{K\pi}, \Delta\phi_{K\pi,\mu\mu})$, (top right) $(m_{K\pi}, \cos\theta_{\psi(2S)})$, (bottom left) $(\cos\theta_{K^{*0}}, \cos\theta_{\psi(2S)})$, (bottom middle) $(\cos\theta_{K^{*0}}, \Delta\phi_{K\pi,\mu\mu})$, and (bottom right) $(\cos\theta_{\psi(2S)}, \Delta\phi_{K\pi,\mu\mu})$. Corrections for the efficiency are applied in the 4D space; the 2D plots allow visualization of their behavior.

weight is assigned to candidates in the signal region; the ratio of the background yield in the signal region and in the sidebands, with a negative sign, is the weight assigned to sideband candidates; and zero weight is assigned to candidates in the remaining regions.

IV. EFFICIENCY AND RESOLUTION

The reconstruction and selection efficiency has been evaluated using simulated samples. The efficiency is calculated as a function of four variables: the $K\pi$ system invariant mass, $m_{K\pi}$; the cosine of the K^{*0} helicity angle, $\cos\theta_{K^{*0}}$; the cosine of the $\psi(2S)$ helicity angle, $\cos\theta_{\psi(2S)}$; and the angle between the $K\pi$ and the $\mu^+\mu^-$ planes calculated in the B^0 rest frame, $\Delta\phi_{K\pi,\mu\mu}$ (this variable is called ϕ in Ref. [12]). The helicity angle of the K^{*0} $[\psi(2S)]$ is defined as the angle between the K^+ (μ^+) direction and the B^0 direction in the K^{*0} $[\psi(2S)]$ rest frame. This four-dimensional (4D) space is subdivided in 24, 25, 5, and 4 bins of the respective variables. The value of the efficiency, at each point of the 4D space, is evaluated as a multilinear interpolation of the values at the 16 bins' centers surrounding it. To the points falling in a border 4D bin, where interpolation is not possible, the value of the efficiency at the bin center is assigned.

To visualize the behavior, 2D efficiency plots are shown, as functions of all the possible variable pairs, in Fig. 2.

Table II lists the resolutions (average uncertainty) of the reconstructed event variables as evaluated on simulated events. They are found to be very small compared to the width of any possible structure searched for in this analysis; therefore, no resolution corrections are applied. In addition, the smooth behavior of the $m_{\psi(2S)\pi}$ resolution, shown in Fig. 3, demonstrates that structures in the $m_{\psi(2S)\pi}$ spectrum could not be caused by resolution effects.

V. K^* RESONANCES

A number of K^{*0} resonances with masses up to slightly above the kinematic limit of 1593 MeV$/c^2$ can decay to the $K\pi$ final state and contribute to the $B^0 \to \psi(2S)K^+\pi^-$ decay. Table III lists these K^{*0} states as well as resonances just above the kinematic limit.

TABLE II. Experimental resolution of kinematical quantities, as estimated from Monte Carlo simulations.

Variable	Resolution
$m_{K\pi}$	1.5 MeV$/c^2$
$m_{\psi(2S)\pi}$	1.8 MeV$/c^2$
$\cos\theta_{K^{*0}}$	0.004
$\cos\theta_{\psi(2S)}$	0.005
$\Delta\phi_{K\pi,\mu\mu}$	0.3°

TABLE III. Mass, width, spin, and parity of resonances known to decay to the $K\pi$ final state [5]. The list is limited to masses up to just above the maximum invariant mass for the $K\pi$ system which, in the decay $B^0 \to \psi(2S)K^+\pi^-$, is 1593 MeV/c^2.

Resonance	Mass (MeV/c^2)	Γ (MeV/c^2)	J^P
$K^*(800)^0$	682 ± 29	547 ± 24	0^+
$K^*(892)^0$	895.81 ± 0.19	47.4 ± 0.6	1^-
$K^*(1410)^0$	1414 ± 15	232 ± 21	1^-
$K_0^*(1430)^0$	1425 ± 50	270 ± 80	0^+
$K_2^*(1430)^0$	1432.4 ± 1.3	109 ± 5	2^+
$K^*(1680)^0$	1717 ± 27	322 ± 110	1^-
$K_3^*(1780)^0$	1776 ± 7	159 ± 21	3^-

The $m_{K\pi}$ spectrum of candidate events, shown in the left plot of Fig. 4, is dominated by the $K^*(892)^0$ meson. A structure in the $K^*(1410)^0$, $K_0^*(1430)^0$, and $K_2^*(1430)^0$ mass regions is also clearly visible. In addition, a nonresonant component is evident. A contribution from the low-mass tail of excited states above the kinematic limit is expected, in particular from the spin-1 $K^*(1680)^0$ and the spin-3 $K_3^*(1780)^0$ due to their large widths. The right plot of Fig. 4 shows the $\cos\theta_{K^{*0}}$ distribution which highlights the rich angular structure of the $K\pi$ system. The resonant structures of the $K\pi$ system can be also seen in the 2D distributions shown in Fig. 5. The plot on the right illustrates how the structures present in the $K\pi$ system considerably influence the $\psi(2S)\pi$ system.

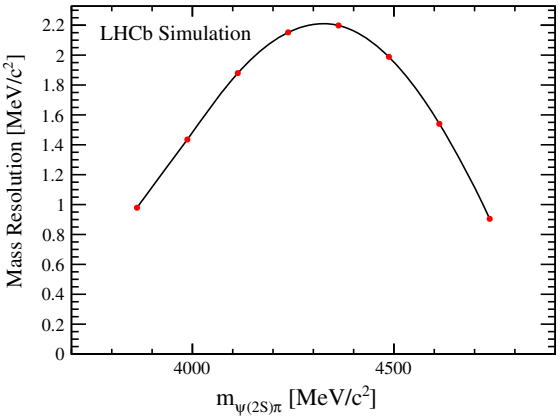

FIG. 3 (color online). The $\psi(2S)\pi$ invariant mass resolution as determined from simulated data (red dots). The continuous line is a spline-based interpolation.

VI. EXTRACTION OF THE MOMENTS OF THE $K\pi$ SYSTEM

Background-subtracted and efficiency-corrected data are subdivided in $m_{K\pi}$ bins of width 30 MeV/c^2, which is suitable for observing the $K\pi$ resonance structures. For each $m_{K\pi}$ bin, the $\cos\theta_{K^{*0}}$ distribution can be expressed as an expansion in terms of Legendre polynomials. The coefficients of this expansion contain all of the information on the angular structure of the system and characterize the spin of the contributing resonances. The angular distribution, after integration over the $\psi(2S)$ decay angles, can be written as

$$\frac{dN}{d\cos\theta_{K^{*0}}} = \sum_{j=0}^{l_{\max}} \langle P_j^U \rangle P_j(\cos\theta_{K^{*0}}), \tag{1}$$

where $l_{\max}$ depends on the maximum orbital angular momentum necessary to describe the $K\pi$ system, $P_j(\cos\theta_{K^{*0}}) = \sqrt{2\pi}Y_j^0(\cos\theta_{K^{*0}})$ are Legendre polynomials, and Y_j^0 are spherical harmonic functions. The coefficients $\langle P_j^U \rangle$ in Eq. (1) are called unnormalized moments (moments, in the following) and can be calculated as integrals of the product of the corresponding Legendre polynomial and the $\cos\theta_{K^{*0}}$ distribution. Resonances of the $K\pi$ system with spin s can contribute to the moments up to $\langle P_{2s}^U \rangle$. Interference between resonances with spin s_1 and s_2 can contribute to moments up to $\langle P_{s_1+s_2}^U \rangle$.

For large samples, the moments are determined from the data as

$$\langle P_j^U \rangle = \sum_{i=1}^{N_{\rm reco}} \frac{W_{\rm signal}^i}{\epsilon^i} P_j(\cos\theta_{K^{*0}}^i), \tag{2}$$

where $N_{\rm reco}$ is the number of reconstructed and selected candidates in the $m_{K\pi}$ bin. The superscript i labels the

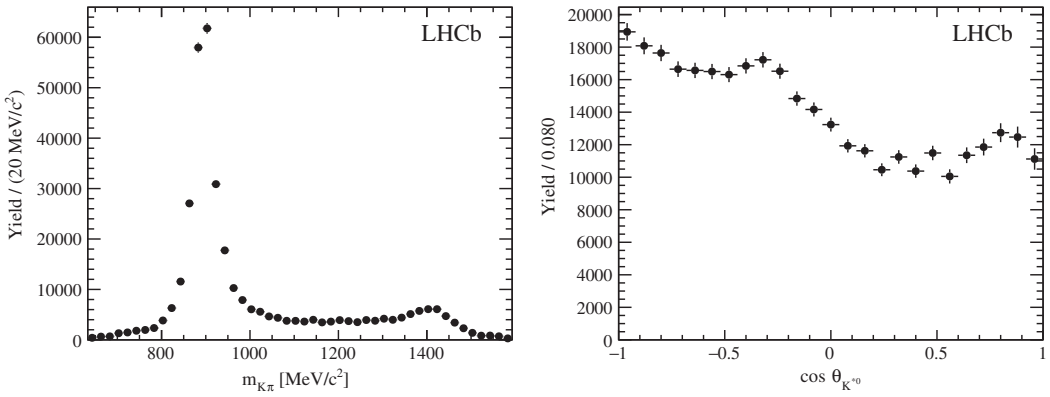

FIG. 4. Distributions of (left) $m_{K\pi}$ and (right) $\cos\theta_{K^{*0}}$, after background subtraction and efficiency correction.

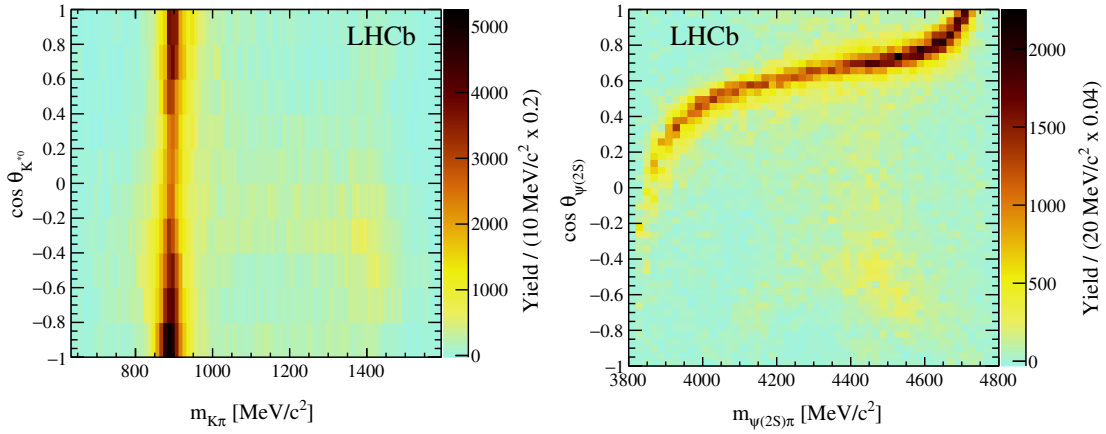

FIG. 5 (color online). The two-dimensional distributions $(m_{K\pi}, \cos\theta_{K^{*0}})$ and $(m_{\psi(2S)\pi}, \cos\theta_{\psi(2S)})$ are shown in the left and the right plots, respectively, after background subtraction and efficiency correction.

candidate, W^i_{signal} is the weight which implements the sideband background subtraction, and $\epsilon^i = \epsilon(m^i_{K\pi}, \cos\theta^i_{K^{*0}}, \cos\theta^i_{\psi(2S)}, \Delta\phi^i_{K\pi,\mu\mu})$ is the efficiency correction, obtained as described in Sec. III.

The dependence of the first six moments on $m_{K\pi}$ is shown in Fig. 6. Together with moment $\langle P^U_0 \rangle$, represented in the left plot of Fig. 4, moments $\langle P^U_2 \rangle$ and $\langle P^U_4 \rangle$ show the S, P, and D wave amplitudes in the mass regions of the $K^*(892)^0$, $K^*(1410)^0$, $K^*_0(1430)^0$, and $K^*_2(1430)^0$ resonances. The behavior of the moment $\langle P^U_6 \rangle$, generated by an F wave, shows that any contribution from $K^*_3(1780)^0$ is small. A resonant $\psi(2S)\pi$ state would, in general, contribute to all $K\pi$ moments.

A detailed discussion of these moments, together with the expressions relating moments to the amplitudes, can be found in Ref. [25] and references therein.

VII. ANALYSIS OF THE $m_{\psi(2S)\pi}$ SPECTRUM

The reflection of the mass and angular structure of the $K\pi$ system into the $\psi(2S)\pi$ invariant mass spectrum is investigated to establish whether it is sufficient to explain the data distribution. This is achieved by comparing the experimental $m_{\psi(2S)\pi}$ spectrum to that of a simulated sample which accounts for the measured mass spectrum and the angular distribution of the $K\pi$ system by means of appropriate weights. The comparison is performed in three

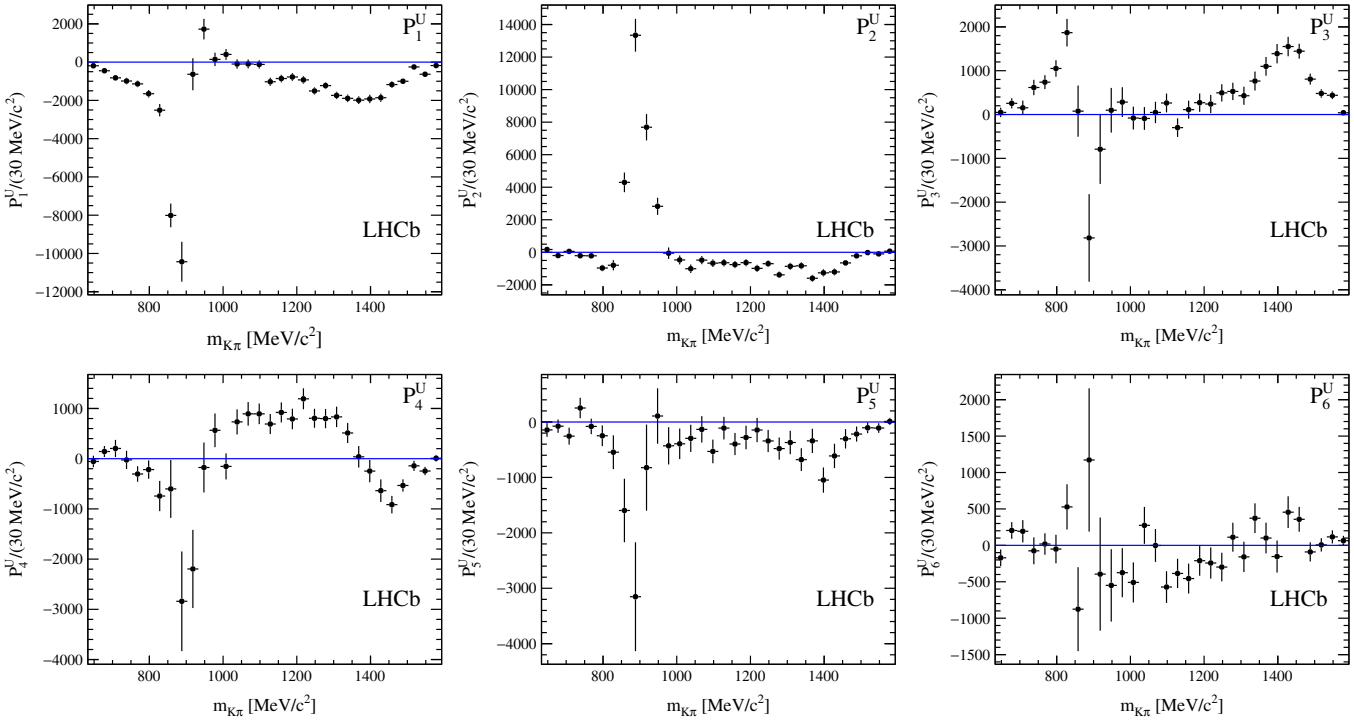

FIG. 6 (color online). Dependence on $m_{K\pi}$ of the first six $K\pi$ moments of the $B^0 \to \psi(2S)K^+\pi^-$ decay mode as determined from data.

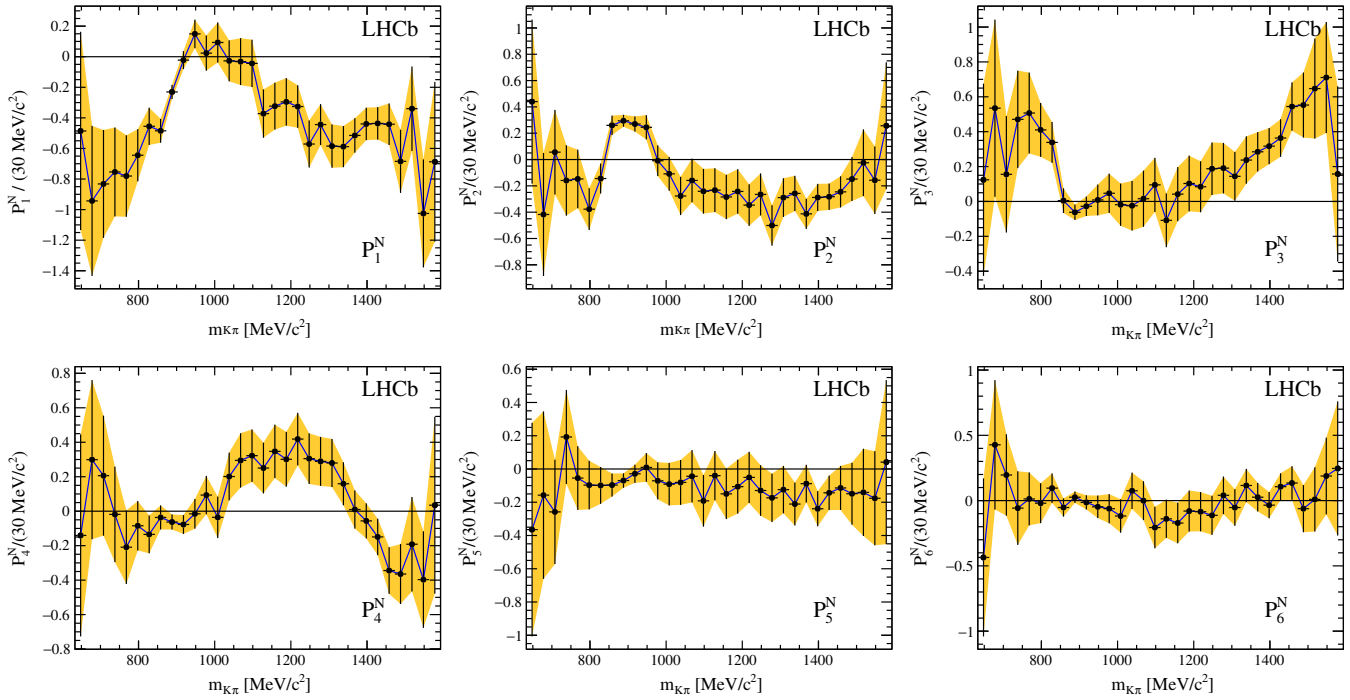

FIG. 7 (color online). First six normalized $K\pi$ moments of the $B^0 \to \psi(2S)K^+\pi^-$ decay mode as a function of $m_{K\pi}$. The shaded (yellow) bands indicate the $\pm 1\sigma$ variations of the moments.

configurations of the $K\pi$ spin contributions. The simplest configuration corresponds to including the contributions of S, P, and D waves, which account for all resonances with mass below the kinematic limit and the $K^*(1680)^0$ meson, just above it (see Table III). In the second configuration, the $K_3^*(1780)^0$ meson is also allowed to contribute. This represents a rather unlikely assumption since it implies a sizeable presence of spin-3 resonances at low $m_{K\pi}$. This configuration can be considered as an extreme case that provides a valuable test for the robustness of the method. In the third configuration, a more realistic choice is made by limiting the maximum spin as a function of $m_{K\pi}$.

For each of the three configurations, 50 million simulated events are generated according to the $B^0 \to \psi(2S)K^+\pi^-$ phase-space decay. The simulation does not include detector effects because it will be compared to efficiency-corrected data. The simulated $m_{K\pi}$ distribution is forced to reproduce the $K\pi$ spectrum in the data (left plot of Fig. 4) by attributing to each event a weight proportional to the ratio between the real and simulated $m_{K\pi}$ spectra in the appropriate bin. Finally, the angular structure of the $K\pi$ system is modified in the simulated sample by applying an additional weight to each event computed as

$$w^i = 1 + \sum_{j=1}^{l_{\max}} \langle P_j^N \rangle P_j(\cos\theta^i_{K^{*0}}), \tag{3}$$

where $\langle P_j^N \rangle = 2\langle P_j^U \rangle / N_{\rm corr}$ are the normalized moments, derived from the moments $\langle P_j^U \rangle$ of Eq. (2), and $N_{\rm corr}$ is the background-subtracted and efficiency-corrected yield of the $m_{K\pi}$ bin where the event lies. The behavior of the first six normalized moments is shown in Fig. 7. The value and the uncertainty of these moments, at a given $m_{K\pi}$ value, are estimated by linearly interpolating adjacent points and their $\pm 1\sigma$ values, respectively, as shown by the shaded (yellow) bands in the figures.

The experimental distribution of the $\psi(2S)\pi$ system invariant mass, $m_{\psi(2S)\pi}$, is shown by the black points in the left plot of Fig. 8.[1] The dotted (black) line represents the pure phase-space simulation; the dash-dotted (red) line shows the effect of the $m_{K\pi}$ modulation; while in the continuous (blue) line, the angular structure of the $K\pi$ system has been taken into account by allowing S, P, and D waves to contribute, which corresponds to setting $l_{\max} = 4$ in Eq. (3). The effect of the angular structure of the $K\pi$ system accounts for most of the features seen in the $m_{\psi(2S)\pi}$ spectrum except for the peak around 4430 MeV/c^2. The dashed (yellow) band in the figure is derived from the $\pm 1\sigma$ values of the normalized moments. The borders of the band are calculated by attributing to each simulated event the weight in Eq. (3) assuming the values of $+1\sigma$ or -1σ, simultaneously for all the contributing normalized moments. Due to the negative contributions of the moments, the borders may cross the central continuous (blue) line. The band should not be considered as an

[1]This plot uses an improved parametrization of the B^0 mass spectrum with respect to Fig. 1 in Ref. [12].

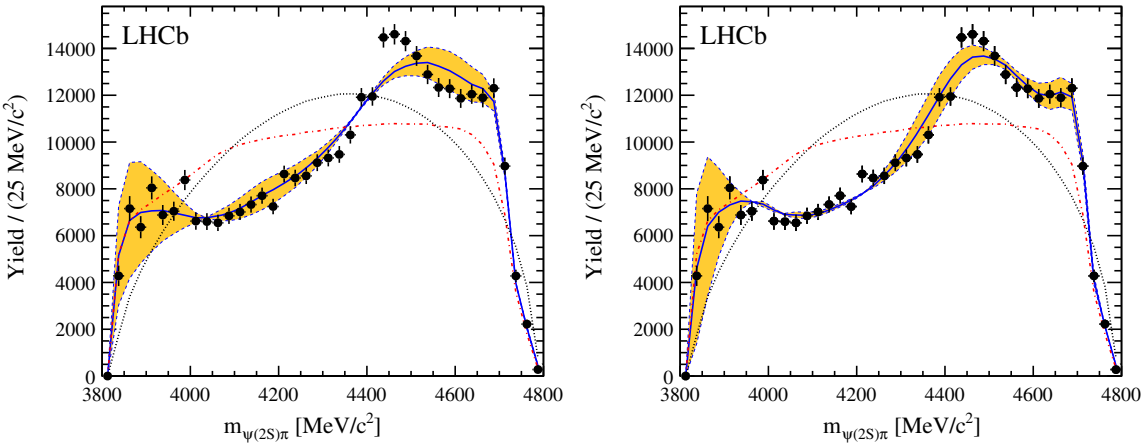

FIG. 8 (color online). Background subtracted and efficiency corrected spectrum of $m_{\psi(2S)\pi}$. Black points represent data. Superimposed are the distributions of the Monte Carlo simulation: the dotted (black) line corresponds to the pure phase-space case; in the dash-dotted (red) line, the $m_{K\pi}$ spectrum is weighted to reproduce the experimental distribution; in the continuous (blue) line, the angular structure of the $K\pi$ system is incorporated using Legendre polynomials up to (left) $l_{\max} = 4$ and (right) $l_{\max} = 6$. The shaded (yellow) bands are related to the uncertainty on normalized moments, which is due to the statistical uncertainty that comes from the data. Therefore, the two uncertainties should not be combined when comparing data and Monte Carlo predictions. See the text for further details.

uncertainty in the simulation but only as an indicative measure of the limited data sample used to compute moments. Since the band and the error bars on the black points are related to the same statistical uncertainty on the data, they should not be combined when estimating the statistical significance of deviations of the data from the prediction.

When spin-3 $K\pi$ states are included, by setting $l_{\max} = 6$, the predicted $m_{\psi(2S)\pi}$ spectrum is modified as shown on the right plot of Fig. 8. Even though the $l_{\max} = 6$ solution apparently provides a better description of the data, it is shown in the following that it is largely incompatible with the data.

In Fig. 9, the maximum Legendre polynomial order is limited as a function of $m_{K\pi}$, according to

$$l_{\max} = \begin{cases} 2 & m_{K\pi} < 836\ \text{MeV}/c^2 \\ 3 & 836\ \text{MeV}/c^2 < m_{K\pi} < 1000\ \text{MeV}/c^2 \\ 4 & m_{K\pi} > 1000\ \text{MeV}/c^2. \end{cases} \quad (4)$$

Figure 9 demonstrates that with this better-motivated $l_{\max}$ assignment, the simulation cannot reproduce adequately the $m_{\psi(2S)\pi}$ distribution.

The disagreement is more evident when looking at the same spectra in different intervals of $m_{K\pi}$, as shown in Fig. 10. Here, the candidates are subdivided according to the $m_{K\pi}$ intervals defined in Eq. (4). The last interval is further split into $1000\ \text{MeV}/c^2 < m_{K\pi} < 1390\ \text{MeV}/c^2$ and $m_{K\pi} > 1390\ \text{MeV}/c^2$. Except for the mass region around $4430\ \text{MeV}/c^2$, all slices exhibit good agreement between the data and the simulation. The peaking structure is particularly evident in the region $1000\ \text{MeV}/c^2 < m_{K\pi} < 1390\ \text{MeV}/c^2$, between the $K^*(892)^0$ and the resonances above $1400\ \text{MeV}/c^2$.

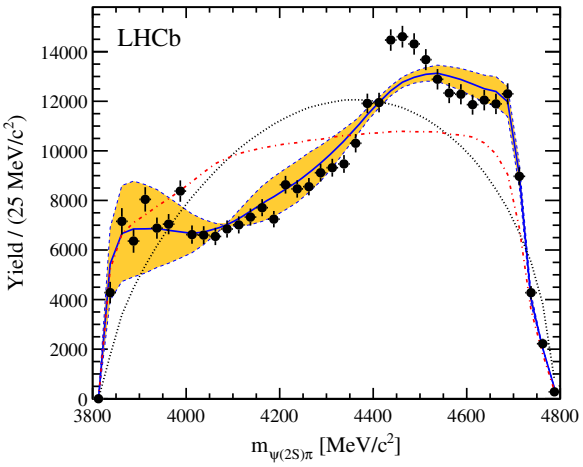

FIG. 9 (color online). The experimental spectrum of $m_{\psi(2S)\pi}$ is shown by the black points. Superimposed are the distributions of the Monte Carlo simulation: the dotted (black) line corresponds to the pure phase-space case; in the dash-dotted (red) line, the $m_{K\pi}$ spectrum is weighted to reproduce the experimental distribution; in the continuous (blue) line, the angular structure of the $K\pi$ system is incorporated using Legendre polynomials with index $l_{\max}$ variable according to $m_{K\pi}$ as described in Eq. (4), reaching up to $l_{\max} = 4$. The shaded (yellow) bands are related to the uncertainty on normalized moments, which is due to the statistical uncertainty that comes from the data. Therefore, the two uncertainties should not be combined when comparing data and Monte Carlo predictions. See the text for further details.

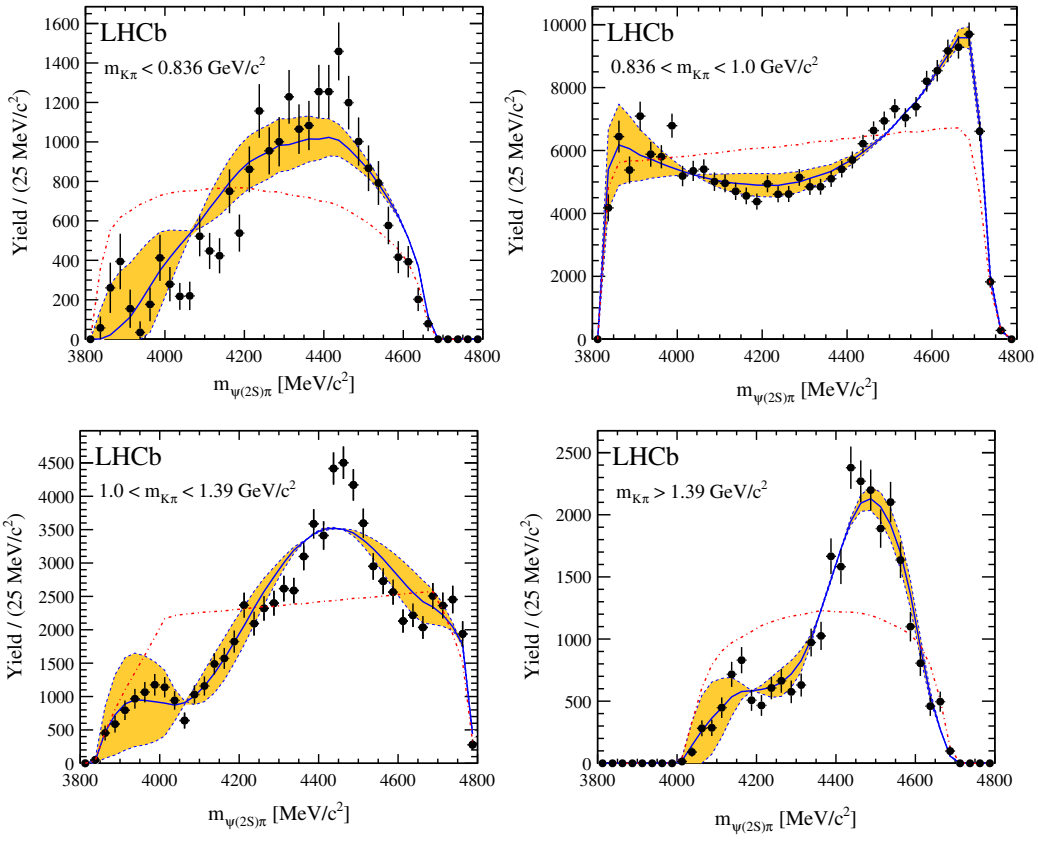

FIG. 10 (color online). Black points represent the experimental distributions of $m_{\psi(2S)\pi}$ for the indicated $m_{K\pi}$ intervals. The dash-dotted (red) line is obtained by modifying the $m_{K\pi}$ spectrum of the phase-space simulation according to the $m_{K\pi}$ experimental spectrum. In the continuous (blue) line, the angular structure of the $K\pi$ system is incorporated using Legendre polynomials with variable index $l_{\max}$ according to Eq. (4). The shaded (yellow) bands are related to the uncertainty on normalized moments, which is due to the statistical uncertainty that comes from the data. Therefore, the two uncertainties should not be combined when comparing data and Monte Carlo predictions. See the text for further details.

VIII. STATISTICAL SIGNIFICANCE OF THE RESULT

The fact that the $m_{\psi(2S)\pi}$ spectrum cannot be explained as a reflection of the angular structure of the $K\pi$ system has been illustrated qualitatively. In this section, the disagreement is quantified via a hypothesis-testing procedure using a likelihood-ratio estimator. The compatibility between the expected $m_{\psi(2S)\pi}$ distribution, accounting for the reflections of the $K\pi$ angular structure, and that observed experimentally is tested for the three $l_{\max}$ assignments described in the previous section, with three sets of about 1000 pseudoexperiments each. For each pseudoexperiment, data and simulated samples involved in the analysis chain are reproduced as pseudosamples, generated at the same statistical level as in the real case. The signal candidate pseudosamples are extracted from a $(m_{K\pi}, \cos\theta_{K^{*0}}, \cos\theta_{\psi(2S)}, \Delta\phi_{K\pi,\mu\mu})$ distribution obtained by an independent EvtGen [35] phase-space sample of $B^0 \to \psi(2S)K^+\pi^-$ events. The distribution is generated, for each of the three $l_{\max}$ cases previously discussed, in order to reproduce the $(m_{K\pi},\cos\theta_{K^{*0}})$ behavior. The background pseudosamples are simulated according to the $(m_{K\pi}, \cos\theta_{K^{*0}}, \cos\theta_{\psi(2S)}, \Delta\phi_{K\pi,\mu\mu})$ distribution of the candidates in the B^0 invariant mass sidebands. Finally, to mimic the calculation of the efficiency correction factors, two additional samples are generated by extracting events from two distributions, in the same 4D space, obtained from the simulation with full detector effects, before and after the application of the analysis chain. The sum of the signal and background samples is then subject to background subtraction and efficiency correction, exactly as for the real data, and moments are calculated. In the pseudoexperiments, events are simulated with equal amounts of each $\psi(2S)$ polarization state. Effects related to $\psi(2S)$ polarization are only included in the pseudosample via their correlation with the $K\pi$ mass and $\cos\theta_{K^{*0}}$ distributions, which are derived from the data. It has been checked that this does not significantly influence the results although the validity of such approximate treatment of $\psi(2S)$ polarization is, in general, analysis dependent and not necessarily appropriate in other experimental situations.

The Monte Carlo method described in Sec. VII is used for each pseudoexperiment to produce an $m_{\psi(2S)\pi}$ probability density function, $\mathcal{F}_{l_{\max}}$, for each of the three $l_{\max}$ configurations. To test for the presence of possible contributions from the $\psi(2S)\pi$ dynamics, which are expected to be present in moments of all orders, a fourth configuration is introduced by setting $l_{\max}$ to the unphysically large value of 30. By including moments up to $l_{\max} = 30$, most of the features of the $m_{\psi(2S)\pi}$ spectrum in data are well described, as can be seen in Fig. 11. The logarithm of the likelihood ratio is used to define the test statistic

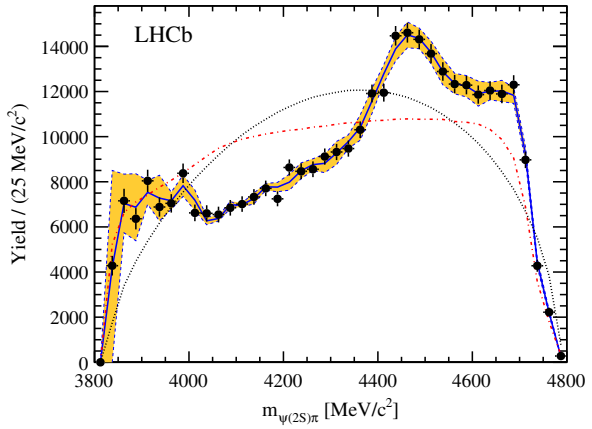

FIG. 11 (color online). The experimental spectrum of $m_{\psi(2S)\pi}$ is shown by the black points. Superimposed are the distributions of the Monte Carlo simulation: the dotted (black) line corresponds to the pure phase space case; in the dash-dotted (red) line, the $m_{K\pi}$ spectrum is weighted to reproduce the experimental distribution; in the continuous (blue) line, the angular structure of the $K\pi$ system is incorporated using Legendre polynomials up to $l_{\max} = 30$, which implies a full description of the spectrum features even if it corresponds to an unphysical configuration of the $K\pi$ system. The shaded (yellow) bands are related to the uncertainty on normalized moments.

$$-2\Delta\mathrm{NLL}_{l_{\max}} = -2\sum_{i=1} \frac{W^i_{\mathrm{signal}}}{\epsilon^i} \log \frac{\mathcal{F}_{l_{\max}}(m^i_{\psi(2S)\pi})}{\mathcal{F}_{30}(m^i_{\psi(2S)\pi})},$$

where the sum runs over the events in the pseudo- or real experiments.

An exotic state in the $\psi(2S)\pi$ system would give contributions to all $K\pi$ Legendre polynomial moments, whereas the conventional $K\pi$ resonances contribute only to moments corresponding to their spin and their interferences. If, for instance, the $B^0 \to \psi(2S)K^+\pi^-$ decay proceeds through S, P, and D $K\pi$ resonances, then only moments with $l_{\max} \leq 4$ would exhibit significant activity. Therefore, activity in moments of order $l_{\max} > 4$ would suggest the presence of other resonant states contributing to the decay. Lower-order $K\pi$ Legendre polynomial moments, determined from data and used to build the prediction, although strongly dominated by the conventional $K\pi$ resonances, could also contain a contribution from the exotic state. As a consequence, a relatively small $\psi(2S)\pi$ resonant contribution could be accommodated by the Monte Carlo prediction. Conversely, a significant disagreement would imply that the $\psi(2S)\pi$ invariant mass spectrum cannot be explained as a reflection of the activity of known resonances in the $K\pi$ system and would therefore constitute strong evidence for the presence of exotic states in the decay $B^0 \to \psi(2S)K^+\pi^-$.

TABLE IV. Significance, S, in units of standard deviations, at which the hypothesis that $m_{\psi(2S)\pi}$ data can be described as a reflection of the $K\pi$ system angular structure is excluded, for different configurations of the $K\pi$ system angular contributions. In the second column, the whole $m_{K\pi}$ spectrum has been analyzed, while in the third one, the specified $m_{K\pi}$ cut is applied.

	S, whole $m_{K\pi}$ spectrum	S, $1.0 < m_{K\pi} < 1.39\,\mathrm{GeV}/c^2$
$l_{\max} = 4$	13.3σ	18.2σ
$l_{\max} = 6$	8.0σ	14.1σ
$l_{\max}(m_{K\pi})$	15.2σ	17.3σ

The $\Delta\mathrm{NLL}_{l_{\max}}$ distributions of the pseudoexperiments are shown in Fig. 12 (points with error bars) for each of the three $l_{\max}$ settings. They are consistent with Gaussian distributions. The statistical significance, S, to rule out the different hypotheses is the distance, in units of standard deviations, between the mean value of the $\Delta\mathrm{NLL}_{l_{\max}}$ (dashed red arrow in Fig. 12) and the observed value of the real experiment (continuous black arrow in Fig. 12). This ranges from 8 to 15 standard deviations, as listed in Table IV.

The table also gives the statistical significance obtained by restricting the analysis to the region $1000\ \mathrm{MeV}/c^2 < m_{K\pi} < 1390\ \mathrm{MeV}/c^2$, where the presence of the structure around the $Z(4430)^-$ mass is most evident, as shown in Fig. 13. Thus, the hypothesis that the data can be explained solely in terms of plausible $K\pi$ degrees of freedom can be

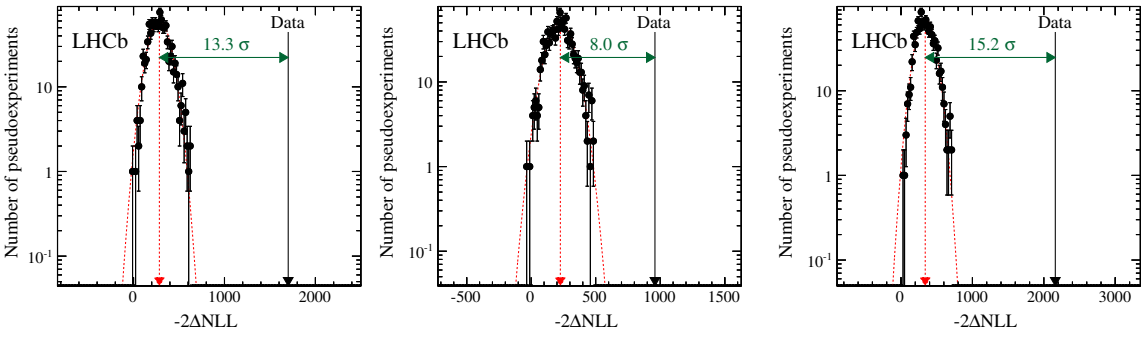

FIG. 12 (color online). Distributions of $-2\Delta\mathrm{NLL}$ for the pseudoexperiments (black dots), fitted with a Gaussian function (dashed red line), in three different configurations of the $K\pi$ system angular contributions: (left) $l_{\max} = 4$, (middle) $l_{\max} = 6$, and (right) $l_{\max}$ variable according to Eq. (4). The black arrow represents the $-2\Delta\mathrm{NLL}$ value obtained on the data.

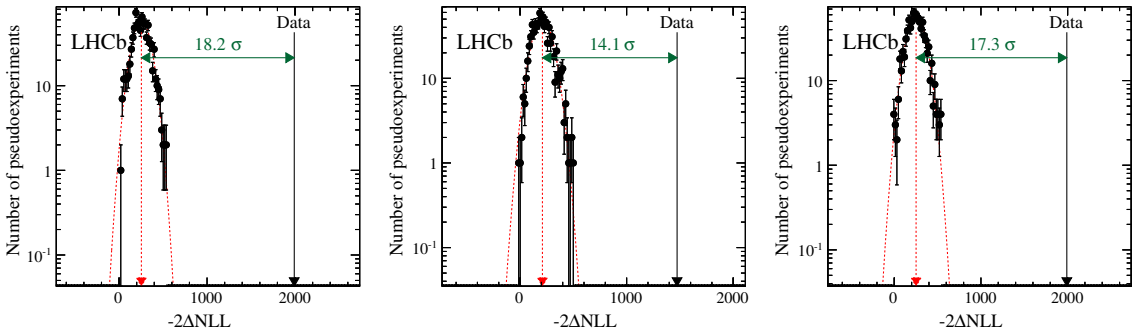

FIG. 13 (color online). Distributions of $-2\Delta\mathrm{NLL}$ for the pseudoexperiments (black dots), fitted with a Gaussian function (dashed red line), for the region 1000 MeV$/c^2 < m_{K\pi} <$ 1390 MeV$/c^2$ in three different configurations of the $K\pi$ system angular contributions: (left) $l_{\max} = 4$, (middle) $l_{\max} = 6$, and (right) $l_{\max}$ variable according to Eq. (4). The black arrow represents the $-2\Delta\mathrm{NLL}$ value obtained on the data.

ruled out without making any assumption on the exact shapes of the $K\pi$ resonances present and their interference patterns.

IX. SUMMARY AND CONCLUSIONS

A satisfactory description of the $\psi(2S)\pi$ mass spectrum in the decay $B^0 \to \psi(2S)K^+\pi^-$ cannot be obtained solely from the reflections of the angular structure of the $K\pi$ system. In particular, a clear peaking structure in the 4430 MeV$/c^2$ mass region remains unexplained. Through a hypothesis-testing procedure based on the likelihood-ratio estimator, compatibility between the data and predictions taking into account the reflections of $K\pi$ states up to spin 3, is excluded with a significance exceeding 8σ. The most plausible configuration, which allows $K\pi$ states with spin values depending on the $K\pi$ mass, is excluded with a significance of more than 15σ.

This work represents an alternative and model-independent confirmation of the existence of a $\psi(2S)\pi$ resonance in the same mass region in which previous model-dependent amplitude analyses have found signals [9,11,12].

ACKNOWLEDGMENTS

We express our gratitude to our colleagues in the CERN accelerator departments for the excellent performance of the LHC. We thank the technical and administrative staff at the LHCb institutes. We acknowledge support from CERN and from the national agencies: CAPES, CNPq, FAPERJ, and FINEP (Brazil); NSFC (China); CNRS/IN2P3 (France); BMBF, DFG, and MPG (Germany); INFN (Italy); FOM and NWO (Netherlands); MNiSW and NCN (Poland); MEN/IFA (Romania); MinES and FANO (Russia); MinECo (Spain); SNSF and SER (Switzerland); NASU (Ukraine); STFC (United Kingdom); and NSF (USA). We acknowledge the computing resources that are provided by CERN, IN2P3 (France), KIT and DESY (Germany), INFN (Italy), SURF (Netherlands), PIC (Spain), GridPP (United Kingdom), RRCKI (Russia), CSCS (Switzerland), IFIN-HH (Romania), CBPF (Brazil), PL-GRID (Poland), and OSC (USA). We are indebted to the communities behind the multiple open source software packages on which we depend. We are also thankful for the computing resources and the access to software research and development tools provided by Yandex, LLC (Russia). Individual groups or members have received support from AvH Foundation (Germany); EPLANET, Marie Skłodowska-Curie Actions, and ERC (European Union); Conseil Général de Haute-Savoie, Labex ENIGMASS, and OCEVU, Région Auvergne (France); RFBR (Russia); XuntaGal and GENCAT (Spain); and The Royal Society and Royal Commission for the Exhibition of 1851 (United Kingdom).

[1] M. Gell-Mann, A schematic model of baryons and mesons, Phys. Lett. **8**, 214 (1964).
[2] A. J. Bevan *et al.* (Belle and *BABAR* Collaborations), The physics of the *B* factories, Eur. Phys. J. C **74**, 3026 (2014).
[3] D. G. Ireland *et al.* (CLAS Collaboration), A Bayesian Analysis of Pentaquark Signals from CLAS Data, Phys. Rev. Lett. **100**, 052001 (2008).
[4] K. H. Hicks, On the conundrum of the pentaquark, Eur. Phys. J. H **37**, 1 (2012).
[5] K. A. Olive *et al.* (Particle Data Group Collaboration), Review of particle physics, Chin. Phys. C **38**, 090001 (2014).
[6] R. Aaij *et al.* (LHCb Collaboration), Evidence for Pentaquark-Charmonium States in $\Lambda_b^0 \to J/\psi p K^-$ Decays, Phys. Rev. Lett. **115**, 07201 (2015).

[7] N. Drenska *et al.*, New hadronic spectroscopy, Riv. Nuovo Cimento **33**, 633 (2010).
[8] S. L. Olsen, A new hadron spectroscopy, Front. Phys. **10**, 121 (2015).
[9] S. K. Choi *et al.* (Belle Collaboration), Observation of a Resonance-Like Structure in the $\pi^{\pm}\psi'$ Mass Distribution in Exclusive $B \to K\pi^{\pm}\psi'$ Decays, Phys. Rev. Lett. **100**, 142001 (2008).
[10] R. Mizuk *et al.* (Belle Collaboration), Dalitz analysis of $B \to K\pi^{+}\psi'$ decays and the $Z(4430)^{+}$, Phys. Rev. D **80**, 031104 (2009).
[11] K. Chilikin *et al.* (Belle Collaboration), Experimental constraints on the spin and parity of the $Z(4430)^{+}$, Phys. Rev. D **88**, 074026 (2013).
[12] R. Aaij *et al.* (LHCb Collaboration), Observation of the Resonant Character of the $Z(4430)^{-}$ State, Phys. Rev. Lett. **112**, 222002 (2014).
[13] J. L. Rosner, Threshold effect and $\pi^{\pm}\psi(2S)$ peak, Phys. Rev. D **76**, 114002 (2007).
[14] E. Braaten and M. Lu, Line shapes of the $Z(4430)$, Phys. Rev. D **79**, 051503 (2009).
[15] K. Cheung, W.-Y. Keung, and T.-C. Yuan, Bottomed analog of $Z^{+}(4433)$, Phys. Rev. D **76**, 117501 (2007).
[16] Y. Li, C.-D. Lu, and W. Wang, Partners of $Z(4430)$ and productions in B decays, Phys. Rev. D **77**, 054001 (2008).
[17] C.-F. Qiao, A uniform description of the states recently observed at B-factories, J. Phys. G **35**, 075008 (2008).
[18] X.-H. Liu, Q. Zhao, and F. E. Close, Search for tetraquark candidate $Z(4430)$ in meson photoproduction, Phys. Rev. D **77**, 094005 (2008).
[19] L. Maiani, A. D. Polosa, and V. Riquer, The charged $Z(4430)$ in the diquark-antidiquark picture, New J. Phys. **10**, 073004 (2008).
[20] D. V. Bugg, How resonances can synchronise with thresholds, J. Phys. G **35**, 075005 (2008).
[21] T. Matsuki, T. Morii, and K. Sudoh, Is the $Z^{+}(4430)$ a radially excited state of D_s?, Phys. Lett. B **669**, 156 (2008).
[22] T. Branz, T. Gutsche, and V. E. Lyubovitskij, Hidden-charm and radiative decays of the $Z(4430)$ as a hadronic $D_1\bar{D}^{*}$ bound state, Phys. Rev. D **82**, 054025 (2010).
[23] G. Galata, Photoproduction of $Z(4430)$ through mesonic Regge trajectories exchange, Phys. Rev. C **83**, 065203 (2011).
[24] M. Nielsen and F. S. Navarra, Charged exotic charmonium states, Mod. Phys. Lett. A **29**, 1430005 (2014).
[25] B. Aubert *et al.* (*BABAR* Collaboration), Search for the $Z(4430)^{-}$ at *BABAR*, Phys. Rev. D **79**, 112001 (2009).
[26] A. A. Alves, Jr. *et al.* (LHCb Collaboration), The LHCb detector at the LHC, J. Instrum. **3**, S08005 (2008).
[27] R. Aaij *et al.* (LHCb Collaboration), LHCb detector performance, Int. J. Mod. Phys. A **30**, 1530022 (2015).
[28] R. Aaij *et al.*, Performance of the LHCb Vertex Locator, J. Instrum. **9**, P09007 (2014).
[29] R. Arink *et al.*, Performance of the LHCb Outer Tracker, J. Instrum. **9**, P01002 (2014).
[30] M. Adinolfi *et al.*, Performance of the LHCb RICH detector at the LHC, Eur. Phys. J. C **73**, 2431 (2013).
[31] A. A. Alves, Jr. *et al.*, Performance of the LHCb muon system, J. Instrum. **8**, P02022 (2013).
[32] R. Aaij *et al.*, The LHCb trigger and its performance in 2011, J. Instrum. **8**, P04022 (2013).
[33] T. Sjöstrand, S. Mrenna, and P. Skands, PYTHIA 6.4 physics and manual, J. High Energy Phys. 05 (2006) 026; T. Sjöstrand, S. Mrenna, and P. Skands, A brief introduction to PYTHIA 8.1, Comput. Phys. Commun. **178**, 852 (2008).
[34] I. Belyaev *et al.*, Handling of the generation of primary events in Gauss, the LHCb simulation framework, J. Phys.: Conf. Ser. **331**, 032047 (2011).
[35] D. J. Lange, The EvtGen particle decay simulation package, Nucl. Instrum. Methods Phys. Res., Sect. A **462**, 152 (2001).
[36] P. Golonka and Z. Was, PHOTOS Monte Carlo: A precision tool for QED corrections in Z and W decays, Eur. Phys. J. C **45**, 97 (2006).
[37] J. Allison *et al.* (Geant4 Collaboration), Geant4 developments and applications, IEEE Trans. Nucl. Sci. **53**, 270 (2006); S. Agostinelli *et al.* (Geant4 Collaboration), Geant4: A simulation toolkit, Nucl. Instrum. Methods Phys. Res., Sect. A **506**, 250 (2003).
[38] M. Clemencic, G. Corti, S. Easo, C. R. Jones, S. Miglioranzi, M. Pappagallo, and P. Robbe, The LHCb simulation application, Gauss: Design, evolution and experience, J. Phys.: Conf. Ser. **331**, 032023 (2011).
[39] A. Hocker *et al.*, TMVA—Toolkit for Multivariate Data Analysis, *Proc. Sci.*, ACAT2007 (2007) 040.
[40] D. Martinez Santos and F. Dupertuis, Mass distributions marginalized over per-event errors, Nucl. Instrum. Methods Phys. Res., Sect. A **764**, 150 (2014).

R. Aaij,[41] B. Adeva,[37] M. Adinolfi,[46] A. Affolder,[52] Z. Ajaltouni,[5] J. Albrecht,[9] F. Alessio,[38] M. Alexander,[51] S. Ali,[41] G. Alkhazov,[30] P. Alvarez Cartelle,[37] A. A. Alves Jr.,[25,38] S. Amato,[2] S. Amerio,[22] Y. Amhis,[7] L. An,[3] L. Anderlini,[17,a] J. Anderson,[40] R. Andreassen,[57] M. Andreotti,[16,b] J. E. Andrews,[58] R. B. Appleby,[54] O. Aquines Gutierrez,[10] F. Archilli,[38] A. Artamonov,[35] M. Artuso,[59] E. Aslanides,[6] G. Auriemma,[25,c] M. Baalouch,[5] S. Bachmann,[11] J. J. Back,[48] A. Badalov,[36] V. Balagura,[31] W. Baldini,[16] R. J. Barlow,[54] C. Barschel,[38] S. Barsuk,[7] W. Barter,[47] V. Batozskaya,[28] Th. Bauer,[41] A. Bay,[39] L. Beaucourt,[4] J. Beddow,[51] F. Bedeschi,[23] I. Bediaga,[1] S. Belogurov,[31] K. Belous,[35] I. Belyaev,[31] E. Ben-Haim,[8] G. Bencivenni,[18] S. Benson,[38] J. Benton,[46] A. Berezhnoy,[32] R. Bernet,[40] M.-O. Bettler,[47] M. van Beuzekom,[41] A. Bien,[11] S. Bifani,[45] T. Bird,[54] A. Bizzeti,[17,d] P. M. Bjørnstad,[54] T. Blake,[48] F. Blanc,[39] J. Blouw,[10] S. Blusk,[59] V. Bocci,[25] A. Bondar,[34] N. Bondar,[30,38] W. Bonivento,[15,38] S. Borghi,[54] A. Borgia,[59] M. Borsato,[7] T. J. V. Bowcock,[52] E. Bowen,[40]

C. Bozzi,[16] T. Brambach,[9] J. van den Brand,[42] J. Bressieux,[39] D. Brett,[54] M. Britsch,[10] T. Britton,[59] J. Brodzicka,[54] N. H. Brook,[46] H. Brown,[52] A. Bursche,[40] G. Busetto,[22,e] J. Buytaert,[38] S. Cadeddu,[15] R. Calabrese,[16,b] M. Calvi,[20,f] M. Calvo Gomez,[36,g] A. Camboni,[36] P. Campana,[18,38] D. Campora Perez,[38] A. Carbone,[14,h] G. Carboni,[24,i] R. Cardinale,[19,38,j] A. Cardini,[15] H. Carranza-Mejia,[50] L. Carson,[50] K. Carvalho Akiba,[2] G. Casse,[52] L. Cassina,[20] L. Castillo Garcia,[38] M. Cattaneo,[38] Ch. Cauet,[9] R. Cenci,[58] M. Charles,[8] Ph. Charpentier,[38] S. Chen,[54] S.-F. Cheung,[55] N. Chiapolini,[40] M. Chrzaszcz,[40,26] K. Ciba,[38] X. Cid Vidal,[38] G. Ciezarek,[53] P. E. L. Clarke,[50] M. Clemencic,[38] H. V. Cliff,[47] J. Closier,[38] V. Coco,[38] J. Cogan,[6] E. Cogneras,[5] P. Collins,[38] A. Comerma-Montells,[11] A. Contu,[15,38] A. Cook,[46] M. Coombes,[46] S. Coquereau,[8] G. Corti,[38] M. Corvo,[16,b] I. Counts,[56] B. Couturier,[38] G. A. Cowan,[50] D. C. Craik,[48] M. Cruz Torres,[60] S. Cunliffe,[53] R. Currie,[50] C. D'Ambrosio,[38] J. Dalseno,[46] P. David,[8] P. N. Y. David,[41] A. Davis,[57] K. De Bruyn,[41] S. De Capua,[54] M. De Cian,[11] J. M. De Miranda,[1] L. De Paula,[2] W. De Silva,[57] P. De Simone,[18] D. Decamp,[4] M. Deckenhoff,[9] L. Del Buono,[8] N. Déléage,[4] D. Derkach,[55] O. Deschamps,[5] F. Dettori,[42] A. Di Canto,[38] H. Dijkstra,[38] S. Donleavy,[52] F. Dordei,[11] M. Dorigo,[39] A. Dosil Suárez,[37] D. Dossett,[48] A. Dovbnya,[43] G. Dujany,[54] F. Dupertuis,[39] P. Durante,[38] R. Dzhelyadin,[35] A. Dziurda,[26] A. Dzyuba,[30] S. Easo,[49,38] U. Egede,[53] V. Egorychev,[31] S. Eidelman,[34] S. Eisenhardt,[50] U. Eitschberger,[9] R. Ekelhof,[9] L. Eklund,[51,38] I. El Rifai,[5] Ch. Elsasser,[40] S. Ely,[59] S. Esen,[11] T. Evans,[55] A. Falabella,[16,b] C. Färber,[11] C. Farinelli,[41] N. Farley,[45] S. Farry,[52] D. Ferguson,[50] V. Fernandez Albor,[37] F. Ferreira Rodrigues,[1] M. Ferro-Luzzi,[38] S. Filippov,[33] M. Fiore,[16,b] M. Fiorini,[16,b] M. Firlej,[27] C. Fitzpatrick,[38] T. Fiutowski,[27] M. Fontana,[10] F. Fontanelli,[19,j] R. Forty,[38] O. Francisco,[2] M. Frank,[38] C. Frei,[38] M. Frosini,[17,38,a] J. Fu,[21,38] E. Furfaro,[24,i] A. Gallas Torreira,[37] D. Galli,[14,h] S. Gallorini,[22] S. Gambetta,[19,j] M. Gandelman,[2] P. Gandini,[59] Y. Gao,[3] J. Garofoli,[59] J. Garra Tico,[47] L. Garrido,[36] C. Gaspar,[38] R. Gauld,[55] L. Gavardi,[9] E. Gersabeck,[11] M. Gersabeck,[54] T. Gershon,[48] Ph. Ghez,[4] A. Gianelle,[22] S. Giani',[39] V. Gibson,[47] L. Giubega,[29] V. V. Gligorov,[38] C. Göbel,[60] D. Golubkov,[31] A. Golutvin,[53,31,38] A. Gomes,[1,k] H. Gordon,[38] C. Gotti,[20] M. Grabalosa Gándara,[5] R. Graciani Diaz,[36] L. A. Granado Cardoso,[38] E. Graugés,[36] G. Graziani,[17] A. Grecu,[29] E. Greening,[55] S. Gregson,[47] P. Griffith,[45] L. Grillo,[11] O. Grünberg,[62] B. Gui,[59] E. Gushchin,[33] Yu. Guz,[35,38] T. Gys,[38] C. Hadjivasiliou,[59] G. Haefeli,[39] C. Haen,[38] S. C. Haines,[47] S. Hall,[53] B. Hamilton,[58] T. Hampson,[46] X. Han,[11] S. Hansmann-Menzemer,[11] N. Harnew,[55] S. T. Harnew,[46] J. Harrison,[54] T. Hartmann,[62] J. He,[38] T. Head,[38] V. Heijne,[41] K. Hennessy,[52] P. Henrard,[5] L. Henry,[8] J. A. Hernando Morata,[37] E. van Herwijnen,[38] M. Heß,[62] A. Hicheur,[1] D. Hill,[55] M. Hoballah,[5] C. Hombach,[54] W. Hulsbergen,[41] P. Hunt,[55] N. Hussain,[55] D. Hutchcroft,[52] D. Hynds,[51] M. Idzik,[27] P. Ilten,[56] R. Jacobsson,[38] A. Jaeger,[11] J. Jalocha,[55] E. Jans,[41] P. Jaton,[39] A. Jawahery,[58] M. Jezabek,[26] F. Jing,[3] M. John,[55] D. Johnson,[55] C. R. Jones,[47] C. Joram,[38] B. Jost,[38] N. Jurik,[59] M. Kaballo,[9] S. Kandybei,[43] W. Kanso,[6] M. Karacson,[38] T. M. Karbach,[38] M. Kelsey,[59] I. R. Kenyon,[45] T. Ketel,[42] B. Khanji,[20] C. Khurewathanakul,[39] S. Klaver,[54] O. Kochebina,[7] M. Kolpin,[11] I. Komarov,[39] R. F. Koopman,[42] P. Koppenburg,[41,38] M. Korolev,[32] A. Kozlinskiy,[41] L. Kravchuk,[33] K. Kreplin,[11] M. Kreps,[48] G. Krocker,[11] P. Krokovny,[34] F. Kruse,[9] M. Kucharczyk,[20,26,38,f] V. Kudryavtsev,[34] K. Kurek,[28] T. Kvaratskheliya,[31] V. N. La Thi,[39] D. Lacarrere,[38] G. Lafferty,[54] A. Lai,[15] D. Lambert,[50] R. W. Lambert,[42] E. Lanciotti,[38] G. Lanfranchi,[18] C. Langenbruch,[38] B. Langhans,[38] T. Latham,[48] C. Lazzeroni,[45] R. Le Gac,[6] J. van Leerdam,[41] J.-P. Lees,[4] R. Lefèvre,[5] A. Leflat,[32] J. Lefrançois,[7] S. Leo,[23] O. Leroy,[6] T. Lesiak,[26] B. Leverington,[11] Y. Li,[3] M. Liles,[52] R. Lindner,[38] C. Linn,[38] F. Lionetto,[40] B. Liu,[15] G. Liu,[38] S. Lohn,[38] I. Longstaff,[51] J. H. Lopes,[2] N. Lopez-March,[39] P. Lowdon,[40] H. Lu,[3] D. Lucchesi,[22,e] H. Luo,[50] A. Lupato,[22] E. Luppi,[16,b] O. Lupton,[55] F. Machefert,[7] I. V. Machikhiliyan,[31] F. Maciuc,[29] O. Maev,[30] S. Malde,[55] G. Manca,[15,l] G. Mancinelli,[6] M. Manzali,[16,b] J. Maratas,[5] J. F. Marchand,[4] U. Marconi,[14] C. Marin Benito,[36] P. Marino,[23,m] R. Märki,[39] J. Marks,[11] G. Martellotti,[25] A. Martens,[8] A. Martín Sánchez,[7] M. Martinelli,[41] D. Martinez Santos,[42] F. Martinez Vidal,[64] D. Martins Tostes,[2] A. Massafferri,[1] R. Matev,[38] Z. Mathe,[38] C. Matteuzzi,[20] A. Mazurov,[16,b] M. McCann,[53] J. McCarthy,[45] A. McNab,[54] R. McNulty,[12] B. McSkelly,[52] B. Meadows,[57,55] F. Meier,[9] M. Meissner,[11] M. Merk,[41] D. A. Milanes,[8] M.-N. Minard,[4] N. Moggi,[14] J. Molina Rodriguez,[60] S. Monteil,[5] D. Moran,[54] M. Morandin,[22] P. Morawski,[26] A. Mordà,[6] M. J. Morello,[23,m] J. Moron,[27] A.-B. Morris,[50] R. Mountain,[59] F. Muheim,[50] K. Müller,[40] R. Muresan,[29] M. Mussini,[14] B. Muster,[39] P. Naik,[46] T. Nakada,[39] R. Nandakumar,[49] I. Nasteva,[2] M. Needham,[50] N. Neri,[21] S. Neubert,[38] N. Neufeld,[38] M. Neuner,[11] A. D. Nguyen,[39] T. D. Nguyen,[39] C. Nguyen-Mau,[39,n] M. Nicol,[7] V. Niess,[5] R. Niet,[9] N. Nikitin,[32] T. Nikodem,[11] A. Novoselov,[35] A. Oblakowska-Mucha,[27] V. Obraztsov,[35] S. Oggero,[41] S. Ogilvy,[51] O. Okhrimenko,[44] R. Oldeman,[15,l] G. Onderwater,[65] M. Orlandea,[29] J. M. Otalora Goicochea,[2] P. Owen,[53] A. Oyanguren,[64] B. K. Pal,[59] A. Palano,[13,o] F. Palombo,[21,p] M. Palutan,[18] J. Panman,[38] A. Papanestis,[49,38] M. Pappagallo,[51] C. Parkes,[54] C. J. Parkinson,[9] G. Passaleva,[17] G. D. Patel,[52] M. Patel,[53] C. Patrignani,[19,j] A. Pazos Alvarez,[37] A. Pearce,[54] A. Pellegrino,[41]

M. Pepe Altarelli,[38] S. Perazzini,[14,h] E. Perez Trigo,[37] P. Perret,[5] M. Perrin-Terrin,[6] L. Pescatore,[45] E. Pesen,[66] K. Petridis,[53] A. Petrolini,[19,j] E. Picatoste Olloqui,[36] B. Pietrzyk,[4] T. Pilař,[48] D. Pinci,[25] A. Pistone,[19] S. Playfer,[50] M. Plo Casasus,[37] F. Polci,[8] A. Poluektov,[48,34] E. Polycarpo,[2] A. Popov,[35] D. Popov,[10] B. Popovici,[29] C. Potterat,[2] A. Powell,[55] J. Prisciandaro,[39] A. Pritchard,[52] C. Prouve,[46] V. Pugatch,[44] A. Puig Navarro,[39] G. Punzi,[23,q] W. Qian,[4] B. Rachwal,[26] J. H. Rademacker,[46] B. Rakotomiaramanana,[39] M. Rama,[18] M. S. Rangel,[2] I. Raniuk,[43] N. Rauschmayr,[38] G. Raven,[42] S. Reichert,[54] M. M. Reid,[48] A. C. dos Reis,[1] S. Ricciardi,[49] A. Richards,[53] M. Rihl,[38] K. Rinnert,[52] V. Rives Molina,[36] D. A. Roa Romero,[5] P. Robbe,[7] A. B. Rodrigues,[1] E. Rodrigues,[54] P. Rodriguez Perez,[54] S. Roiser,[38] V. Romanovsky,[35] A. Romero Vidal,[37] M. Rotondo,[22] J. Rouvinet,[39] T. Ruf,[38] F. Ruffini,[23] H. Ruiz,[36] P. Ruiz Valls,[64] G. Sabatino,[25,i] J. J. Saborido Silva,[37] N. Sagidova,[30] P. Sail,[51] B. Saitta,[15,l] V. Salustino Guimaraes,[2] C. Sanchez Mayordomo,[64] B. Sanmartin Sedes,[37] R. Santacesaria,[25] C. Santamarina Rios,[37] E. Santovetti,[24,i] M. Sapunov,[6] A. Sarti,[18,r] C. Satriano,[25,c] A. Satta,[24] M. Savrie,[16,b] D. Savrina,[31,32] M. Schiller,[42] H. Schindler,[38] M. Schlupp,[9] M. Schmelling,[10] B. Schmidt,[38] O. Schneider,[39] A. Schopper,[38] M.-H. Schune,[7] R. Schwemmer,[38] B. Sciascia,[18] A. Sciubba,[25] M. Seco,[37] A. Semennikov,[31] K. Senderowska,[27] I. Sepp,[53] N. Serra,[40] J. Serrano,[6] L. Sestini,[22] P. Seyfert,[11] M. Shapkin,[35] I. Shapoval,[16,43,b] Y. Shcheglov,[30] T. Shears,[52] L. Shekhtman,[34] V. Shevchenko,[63] A. Shires,[9] R. Silva Coutinho,[48] G. Simi,[22] M. Sirendi,[47] N. Skidmore,[46] T. Skwarnicki,[59] N. A. Smith,[52] E. Smith,[55,49] E. Smith,[53] J. Smith,[47] M. Smith,[54] H. Snoek,[41] M. D. Sokoloff,[57] F. J. P. Soler,[51] F. Soomro,[39] D. Souza,[46] B. Souza De Paula,[2] B. Spaan,[9] A. Sparkes,[50] F. Spinella,[23] P. Spradlin,[51] F. Stagni,[38] S. Stahl,[11] O. Steinkamp,[40] O. Stenyakin,[35] S. Stevenson,[55] S. Stoica,[29] S. Stone,[59] B. Storaci,[40] S. Stracka,[23,38] M. Straticiuc,[29] U. Straumann,[40] R. Stroili,[22] V. K. Subbiah,[38] L. Sun,[57] W. Sutcliffe,[53] K. Swientek,[27] S. Swientek,[9] V. Syropoulos,[42] M. Szczekowski,[28] P. Szczypka,[39,38] D. Szilard,[2] T. Szumlak,[27] S. T'Jampens,[4] M. Teklishyn,[7] G. Tellarini,[16,b] F. Teubert,[38] C. Thomas,[55] E. Thomas,[38] J. van Tilburg,[41] V. Tisserand,[4] M. Tobin,[39] S. Tolk,[42] L. Tomassetti,[16,b] D. Tonelli,[38] S. Topp-Joergensen,[55] N. Torr,[55] E. Tournefier,[4] S. Tourneur,[39] M. T. Tran,[39] M. Tresch,[40] A. Tsaregorodtsev,[6] P. Tsopelas,[41] N. Tuning,[41] M. Ubeda Garcia,[38] A. Ukleja,[28] A. Ustyuzhanin,[63] U. Uwer,[11] V. Vagnoni,[14] G. Valenti,[14] A. Vallier,[7] R. Vazquez Gomez,[18] P. Vazquez Regueiro,[37] C. Vázquez Sierra,[37] S. Vecchi,[16] J. J. Velthuis,[46] M. Veltri,[17,s] G. Veneziano,[39] M. Vesterinen,[11] B. Viaud,[7] D. Vieira,[2] M. Vieites Diaz,[37] X. Vilasis-Cardona,[36,g] A. Vollhardt,[40] D. Volyanskyy,[10] D. Voong,[46] A. Vorobyev,[30] V. Vorobyev,[34] C. Voß,[62] H. Voss,[10] J. A. de Vries,[41] R. Waldi,[62] C. Wallace,[48] R. Wallace,[12] J. Walsh,[23] S. Wandernoth,[11] J. Wang,[59] D. R. Ward,[47] N. K. Watson,[45] D. Websdale,[53] M. Whitehead,[48] J. Wicht,[38] D. Wiedner,[11] G. Wilkinson,[55] M. P. Williams,[45] M. Williams,[56] F. F. Wilson,[49] J. Wimberley,[58] J. Wishahi,[9] W. Wislicki,[28] M. Witek,[26] G. Wormser,[7] S. A. Wotton,[47] S. Wright,[47] S. Wu,[3] K. Wyllie,[38] Y. Xie,[61] Z. Xing,[59] Z. Xu,[39] Z. Yang,[3] X. Yuan,[3] O. Yushchenko,[35] M. Zangoli,[14] M. Zavertyaev,[10,t] F. Zhang,[3] L. Zhang,[59] W. C. Zhang,[12] Y. Zhang,[3] A. Zhelezov,[11] A. Zhokhov,[31] L. Zhong,[3] and A. Zvyagin[38]

(LHCb Collaboration)

[1]*Centro Brasileiro de Pesquisas Físicas (CBPF), Rio de Janeiro, Brazil*
[2]*Universidade Federal do Rio de Janeiro (UFRJ), Rio de Janeiro, Brazil*
[3]*Center for High Energy Physics, Tsinghua University, Beijing, China*
[4]*LAPP, Université de Savoie, CNRS/IN2P3, Annecy-Le-Vieux, France*
[5]*Clermont Université, Université Blaise Pascal, CNRS/IN2P3, LPC, Clermont-Ferrand, France*
[6]*CPPM, Aix-Marseille Université, CNRS/IN2P3, Marseille, France*
[7]*LAL, Université Paris-Sud, CNRS/IN2P3, Orsay, France*
[8]*LPNHE, Université Pierre et Marie Curie, Université Paris Diderot, CNRS/IN2P3, Paris, France*
[9]*Fakultät Physik, Technische Universität Dortmund, Dortmund, Germany*
[10]*Max-Planck-Institut für Kernphysik (MPIK), Heidelberg, Germany*
[11]*Physikalisches Institut, Ruprecht-Karls-Universität Heidelberg, Heidelberg, Germany*
[12]*School of Physics, University College Dublin, Dublin, Ireland*
[13]*Sezione INFN di Bari, Bari, Italy*
[14]*Sezione INFN di Bologna, Bologna, Italy*
[15]*Sezione INFN di Cagliari, Cagliari, Italy*
[16]*Sezione INFN di Ferrara, Ferrara, Italy*
[17]*Sezione INFN di Firenze, Firenze, Italy*
[18]*Laboratori Nazionali dell'INFN di Frascati, Frascati, Italy*
[19]*Sezione INFN di Genova, Genova, Italy*

[20]*Sezione INFN di Milano Bicocca, Milano, Italy*
[21]*Sezione INFN di Milano, Milano, Italy*
[22]*Sezione INFN di Padova, Padova, Italy*
[23]*Sezione INFN di Pisa, Pisa, Italy*
[24]*Sezione INFN di Roma Tor Vergata, Roma, Italy*
[25]*Sezione INFN di Roma La Sapienza, Roma, Italy*
[26]*Henryk Niewodniczanski Institute of Nuclear Physics Polish Academy of Sciences, Kraków, Poland*
[27]*AGH - University of Science and Technology, Faculty of Physics and Applied Computer Science, Kraków, Poland*
[28]*National Center for Nuclear Research (NCBJ), Warsaw, Poland*
[29]*Horia Hulubei National Institute of Physics and Nuclear Engineering, Bucharest-Magurele, Romania*
[30]*Petersburg Nuclear Physics Institute (PNPI), Gatchina, Russia*
[31]*Institute of Theoretical and Experimental Physics (ITEP), Moscow, Russia*
[32]*Institute of Nuclear Physics, Moscow State University (SINP MSU), Moscow, Russia*
[33]*Institute for Nuclear Research of the Russian Academy of Sciences (INR RAN), Moscow, Russia*
[34]*Budker Institute of Nuclear Physics (SB RAS) and Novosibirsk State University, Novosibirsk, Russia*
[35]*Institute for High Energy Physics (IHEP), Protvino, Russia*
[36]*Universitat de Barcelona, Barcelona, Spain*
[37]*Universidad de Santiago de Compostela, Santiago de Compostela, Spain*
[38]*European Organization for Nuclear Research (CERN), Geneva, Switzerland*
[39]*Ecole Polytechnique Fédérale de Lausanne (EPFL), Lausanne, Switzerland*
[40]*Physik-Institut, Universität Zürich, Zürich, Switzerland*
[41]*Nikhef National Institute for Subatomic Physics, Amsterdam, The Netherlands*
[42]*Nikhef National Institute for Subatomic Physics and VU University Amsterdam, Amsterdam, The Netherlands*
[43]*NSC Kharkiv Institute of Physics and Technology (NSC KIPT), Kharkiv, Ukraine*
[44]*Institute for Nuclear Research of the National Academy of Sciences (KINR), Kyiv, Ukraine*
[45]*University of Birmingham, Birmingham, United Kingdom*
[46]*H.H. Wills Physics Laboratory, University of Bristol, Bristol, United Kingdom*
[47]*Cavendish Laboratory, University of Cambridge, Cambridge, United Kingdom*
[48]*Department of Physics, University of Warwick, Coventry, United Kingdom*
[49]*STFC Rutherford Appleton Laboratory, Didcot, United Kingdom*
[50]*School of Physics and Astronomy, University of Edinburgh, Edinburgh, United Kingdom*
[51]*School of Physics and Astronomy, University of Glasgow, Glasgow, United Kingdom*
[52]*Oliver Lodge Laboratory, University of Liverpool, Liverpool, United Kingdom*
[53]*Imperial College London, London, United Kingdom*
[54]*School of Physics and Astronomy, University of Manchester, Manchester, United Kingdom*
[55]*Department of Physics, University of Oxford, Oxford, United Kingdom*
[56]*Massachusetts Institute of Technology, Cambridge, Massachusetts, USA*
[57]*University of Cincinnati, Cincinnati, Ohio, USA*
[58]*University of Maryland, College Park, Maryland, USA*
[59]*Syracuse University, Syracuse, New York, USA*
[60]*Pontifícia Universidade Católica do Rio de Janeiro (PUC-Rio), Rio de Janeiro, Brazil (associated with Institution Universidade Federal do Rio de Janeiro (UFRJ), Rio de Janeiro, Brazil)*
[61]*Institute of Particle Physics, Central China Normal University, Wuhan, Hubei, China (associated with Institution Center for High Energy Physics, Tsinghua University, Beijing, China)*
[62]*Institut für Physik, Universität Rostock, Rostock, Germany (associated with Institution Physikalisches Institut, Ruprecht-Karls-Universität Heidelberg, Heidelberg, Germany)*
[63]*National Research Centre Kurchatov Institute, Moscow, Russia (associated with Institution Institute of Theoretical and Experimental Physics (ITEP), Moscow, Russia)*
[64]*Instituto de Fisica Corpuscular (IFIC), Universitat de Valencia-CSIC, Valencia, Spain (associated with Institution Universitat de Barcelona, Barcelona, Spain)*
[65]*KVI - University of Groningen, Groningen, The Netherlands (associated with Institution Nikhef National Institute for Subatomic Physics, Amsterdam, The Netherlands)*
[66]*Celal Bayar University, Manisa, Turkey (associated with Institution European Organization for Nuclear Research (CERN), Geneva, Switzerland)*

[a]Also at Università di Firenze, Firenze, Italy.
[b]Also at Università di Ferrara, Ferrara, Italy.
[c]Also at Università della Basilicata, Potenza, Italy.

[d]Also at Università di Modena e Reggio Emilia, Modena, Italy.
[e]Also at Università di Padova, Padova, Italy.
[f]Also at Università di Milano Bicocca, Milano, Italy.
[g]Also at LIFAELS, La Salle, Universitat Ramon Llull, Barcelona, Spain.
[h]Also at Università di Bologna, Bologna, Italy.
[i]Also at Università di Roma Tor Vergata, Roma, Italy.
[j]Also at Università di Genova, Genova, Italy.
[k]Also at Universidade Federal do Triângulo Mineiro (UFTM), Uberaba-MG, Brazil.
[l]Also at Università di Cagliari, Cagliari, Italy.
[m]Also at Scuola Normale Superiore, Pisa, Italy.
[n]Also at Hanoi University of Science, Hanoi, Viet Nam.
[o]Also at Università di Bari, Bari, Italy.
[p]Also at Università degli Studi di Milano, Milano, Italy.
[q]Also at Università di Pisa, Pisa, Italy.
[r]Also at Università di Roma La Sapienza, Roma, Italy.
[s]Also at Università di Urbino, Urbino, Italy.
[t]Also at P.N. Lebedev Physical Institute, Russian Academy of Science (LPI RAS), Moscow, Russia.